Brodogradnja Volume 77 Number 4 (2026) 77401

journal homepage: www.brodogradnja.fsb.hr

Brodogradnja

An International Journal of Naval Architecture and Ocean Engineering for Research and Development

Numerical study on the effect of vortex generator geometry and placement on single-blade performance in vertical axis current turbines

Daif Rahuna[1,2], *I Ketut Aria Pria Utama*[3,*], *Erwandi Erwandi*[2], *Dendy Satrio*[1]

[1]*Department of Ocean Engineering, Faculty of Marine Technology, Institut Teknologi Sepuluh Nopember (ITS), Surabaya 60111, Indonesia*
[2]*Research Center for Hydrodynamic Technology (PRTH), Research Organization for Energy and Manufacture (OREM), National Research and Innovation Agency (BRIN), Indonesia*
[3]*Department of Naval Architecture, Faculty of Marine Technology, Institut Teknologi Sepuluh Nopember (ITS), Surabaya 60111, Indonesia*

ARTICLE INFO

Keywords:
Drag Coefficient (C_D)
Lift Coefficient (C_L)
NACA 0021
Rectangular VG
Trapezoidal VG

ABSTRACT

This study investigates the effect of adding vortex generators (VGs) to a single NACA 0021 blade applied in vertical axis current turbines (VACTs). The focus is on rectangular and trapezoidal VG shapes and their placement between 10 and 30 % of the chord length on the hydrofoil surface. CFD analyses were carried out under steady state conditions using the Reynolds-Averaged Navier–Stokes (RANS) approach, coupled with the *k-ω* SST turbulence model. The results demonstrate performance improvements of the hydrofoil with the inclusion of VGs. Specifically, rectangular VGs positioned at 10 % of the chord length increased the average lift coefficient (C_L) by 31.5 % and reduced the average drag coefficient (C_D) by 8 %. Similarly, trapezoidal VGs placed at 15 % of the chord length increased C_L by 29.5 % and decreased C_D by 7.1 %. Optimizing the geometry and placement of VGs can significantly enhance turbine efficiency by improving boundary layer control and delaying flow separation.

1. Introduction

In general, vertical axis current turbines (VACTs) exhibit several limitations, notably low power conversion efficiency, poor self-starting capability, susceptibility to cavitation, and structural vibrations [1, 2]. Nevertheless, they offer distinct advantages such as omnidirectional flow acceptance, ease of maintenance, low manufacturing cost, and a straightforward design. These favorable attributes have continued to attract research attention, prompting numerous studies in recent decades focused on enhancing VACT performance.

A considerable body of research has focused on enhancing the self-starting capability of VACTs, with particular attention to flow control strategies. In parallel, various flow augmentation devices have been employed to modify the fluid dynamics around VACTs, including flow perturbation mechanisms [3, 4], deflector systems [5], tubercle modifications [6, 7], and vortex generators (VGs), the latter being the primary focus of this study.

* Corresponding author.
E-mail address: kutama@its.ac.id

https://doi.org/10.21278/brod77401
Received 17 June 2025; Received in revised form 13 March 2026; Accepted 16 March 2026
Available online 30 March 2026
ISSN 0007-215X; eISSN 1845-5859

Flow control approaches can be utilized to prevent boundary layer (BL) separation and stalling. Vortex generators were originally proposed by Taylor [8] to increase lift and decrease drag by delaying stall at an aircraft's wing, in aviation [9]. When VG is on the upper surface of the wing, it helps maintain airflow attachment to the wing at high angles of attack (α), reducing stall speed and/or making the control surfaces more effective. The Boeing 737 utilizes VG devices not only on the wings but also on the horizontal stabilizer and the forward fuselage. The addition of VGs serves to stabilize airflow over the vertical and horizontal stabilizers, help control airflow at high speeds, and reduce aerodynamic noise that could disturb the pilot [10].

VGs are considered one of the most effective methods for enhancing the performance of horizontal axis wind turbines (HAWTs), due to their strong flow control capabilities, low cost, and ease of implementation [11]. VGs function by transferring momentum from the free-stream flow into the near-wall region, thereby increasing the momentum in this area, which helps delay or prevent flow separation from the blade surface in smooth blade configurations [12]. This flow separation, commonly referred to as dynamic stall, is a transient and unstable aerodynamic phenomenon. Moreover, VGs can help mitigate adverse effects such as vibration, noise, and fatigue stresses induced by stall events, leading to improved aerodynamic performance and increased energy output. These advantages have made VGs the subject of considerable research interest in recent years [1, 2].

Recent studies on VGs have increasingly focused on understanding the underlying flow mechanisms and developing effective VG design methodologies to optimize their performance on various airfoil types. Optimal VG design is often determined based on parameters such as vortex strength, vorticity trajectories, geometric dimensions, and free-stream velocity. The size, placement, and configuration of VGs play a critical role in promoting early vortex formation, which in turn enhances airfoil aerodynamic performance [13, 14]. However, these investigations also indicate that no single VG model has consistently outperformed others in representing the influence of VGs on the flow field when modeled using body force approaches [13, 15].

Mueller-Vahl et al. [16] demonstrated that decreasing the spacing between VGs not only delayed flow separation by up to 12.5° beyond the conventional stall α and increased the maximum lift coefficient (C_{Lmax}) by 31 % but also contributed to a reduction in drag coefficient (C_D). The enhanced vortex interaction due to tighter VG spacing promotes the outward migration of vortex cores from the airfoil surface, improving flow attachment. In a related study on the DU97-W-300 airfoil, VG chordwise position and height were identified as the dominant factors influencing aerodynamic performance, whereas parameters such as VG length, pitch angle, geometry, and spanwise distribution exhibited comparatively minor effects [17]. Complementary CFD investigations on the NREL S809 airfoil further revealed that implementing a dual-row arrangement of rectangular VGs significantly improved flow separation control, yielding an increase in C_{Lmax} of 0.27 over a single-row configuration positioned near the leading edge [18].

Yan et al. [19] conducted a CFD analysis based on the Reynolds-Averaged Navier–Stokes (RANS) and unsteady RANS (URANS) approaches using the k–ω Shear Stress Transport (SST) turbulence model [20, 21]. The objective of their study was to evaluate the aerodynamic effects of adding micro–vortex generators (micro-VGs) to the NACA 0018 airfoil blade of a vertical axis wind turbine (VAWT). The simulation results demonstrated that an optimal micro-VG configuration can effectively energize the boundary layer, delay flow separation (stall), and enhance aerodynamic stability across various α.

Satrio et al. [20] conducted a CFD analysis using ANSYS CFX based on the URANS approach with the k–ω SST turbulence model. The objective of the study was to evaluate the hydrodynamic performance of triangular VGs integrated into a vertical axis ocean current turbine (VAOCT) employing a NACA 0021 hydrofoil profile. The results revealed that the addition of VGs significantly enhanced the lift characteristics and effectively delayed stall occurrence, thereby improving the overall efficiency of the turbine under low ocean current conditions. The integration of VGs on the VAOCT blades also increased the power coefficient and delivered better performance under realistic, fluctuating flow conditions, making it a valuable enhancement for optimizing renewable energy systems based on ocean and river currents [21, 22].

Numerical investigations have been extensively carried out to assess the influence of VG implementation on both airfoil and turbine performance [23, 24]. Although high-fidelity approaches such as Direct Numerical Simulation (DNS) and Large Eddy Simulation (LES) are utilized in some studies, the RANS

method remains the most commonly applied due to its balance between accuracy and computational efficiency [5, 7]. To avoid the computational expense associated with resolving detailed VG geometries using fine meshes, researchers have widely adopted simplified VG modeling techniques [3]. This improves lift production, reduces drag, and enhances the turbine's overall power output and efficiency, particularly at low to moderate flow velocities. Research has shown that integrating VGs into the blades of VACTs leads to increased power coefficients and better performance under real world, fluctuating flow conditions, making them a valuable addition for optimizing renewable marine and river current energy systems [23, 24].

The limitations of this research lie in the two micro-VG shapes-rectangular and trapezoidal, each with a height equivalent to the local boundary layer thickness at the installation location, a single-row configuration, and positioned at 10 %, 15 %, 20 %, 25 %, and 30 % of the chord length. Numerical simulations are performed using a Computational Fluid Dynamics (CFD) approach in ANSYS Fluent, based on the RANS equations with the *k–ω SST* turbulence model. The innovation of this research lies in the integration of micro-vortex generators (micro-VGs) with rectangular and trapezoidal shapes into a single NACA 0021 profile blade, as a VAOCT blade of the H-Darrieus type. The goal is to improve the hydrodynamic performance of turbine blades by effectively delaying flow separation (stalling), increasing lift generation, and reducing drag.

2. Methodology

This study utilizes a numerical simulation framework centred on a single-blade model, representing an isolated hydrofoil element rather than a full multi-blade turbine system as encountered in real-world applications. The analysis is conducted on a baseline symmetric NACA 0021 hydrofoil, evaluated in both clean and VG, modified configurations. Both rectangular and trapezoidal VGs are employed, with variations in their placement along the hydrofoil surface to assess their influence on hydrodynamic performance. The primary aim of the simulation is to offer preliminary insights into the effects of VG integration, including comparative assessments of configurations with and without VGs, and to evaluate how VG geometry and positioning impact stall delay, lift coefficient (C_L), C_D, and dynamic flow structures in proximity to the hydrofoil surface.

This section outlines the methodology of the study, providing a structured framework to evaluate the impact of VG integration on the hydrodynamic performance of the NACA 0021 hydrofoil, which serves as a blade in a VACT system. The first step involves defining the geometry and preparing the computational domain, which is detailed comprehensively. The subsequent stages include mesh generation, grid independence testing, boundary condition setup, and solver configuration. The validation process includes evaluating solver settings and performing remeshing if the results deviate from expected validation trends. The implementation of rectangular and trapezoidal VGs will only proceed once the validation criteria are satisfactorily met. The results section presents the outcomes for two primary hydrodynamic parameters: C_L and C_D. Additionally, a contour analysis of the flow behaviour around the hydrofoil is conducted, comparing configurations with and without VGs. The final section of the study offers a performance prediction for VG implementation on VACT, focusing on the specific application of VGs on the NACA 0021 hydrofoil within the VACT configuration.

2.1 Model Geometry

In VACT Type-H turbines, the blades are typically designed using symmetrical hydrofoil profiles, which enable them to sustain lift generation on both surfaces during the entire rotational cycle. The NACA 0021 hydrofoil is characterized by a maximum thickness of 21 %*c*, positioned at 30 %*c* from the leading edge. This hydrofoil also exhibits a maximum C_L of 0.98 [25], indicating its capability to generate sufficient lift under various flow conditions. This characteristic makes it a suitable choice for applications in vertical-axis current turbines, where consistent hydrodynamic performance is essential throughout the rotational cycle. In the present study, VGs are implemented on hydrofoils to examine their functional effects, comparing the performance of hydrofoils both with and without VGs. The VGs employed include single-row arrays of rectangular and trapezoidal shapes, as well as counter-rotating configurations.

Augmentation devices, such as VGs, are employed to modify the fluid flow behaviour around Type-H VACTs by strategically altering the boundary layer dynamics. In this study, VGs are mounted on the blade surface in spanwise pairs [26], as illustrated in Figure 1. The effectiveness of VG integration in promoting vortex formation, delaying flow separation (stall), enhancing lift, and reducing drag is highly dependent on several factors, including the VG's dimensions, placement, configuration, and the specific hydrofoil profile used. According to Paraschivoiu [27], the Darrieus turbine, which drives the VACT, is a lift-driven device. Increasing lift performance is expected to improve turbine efficiency and self-starting capability. These parameters must be carefully optimized to ensure that the induced vortices effectively re-energize the boundary layer, thereby maintaining attached flow over a wider range of α. Improper VG placement or sizing can lead to adverse flow interactions, potentially increasing drag without significant lift enhancement. Therefore, a detailed numerical investigation is essential to evaluate the hydrodynamic impacts of VG implementation and to determine optimal design strategies tailored to the NACA 0021 hydrofoil operating within a VACT configuration.

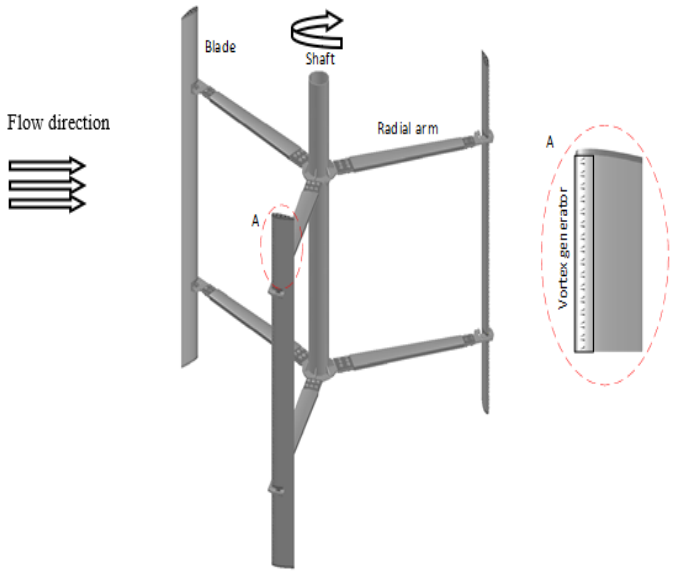

Fig. 1 Vertical axis current ocean turbine, H-Darrieus type with vortex generators [14]

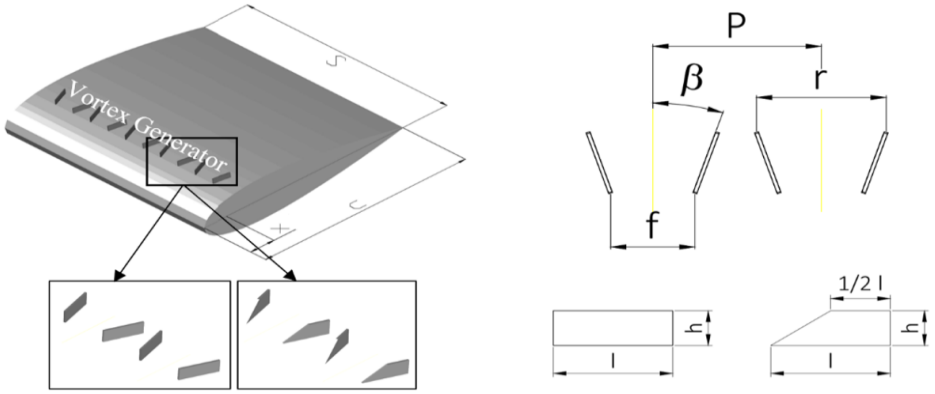

Fig. 2 Schematic of the vane-type vortex generators [20]

These parameters are systematically varied to assess their influence on flow separation control and hydrodynamic performance. The placement range between 10 %c and 30 %c, with intervals of 5 %, was selected based on prior studies indicating that early boundary layer interaction significantly affects stall delay and lift enhancement [19, 20]. The use of a single-row, counter-rotating configuration is intended to generate strong, stable vortices that promote boundary layer attachment without introducing excessive drag. Geometric details of the VGs, including height-to-chord ratio (h/c), length-to-height ratio (l/h), inter-VG spacing (p/h),

and the upstream and downstream distances (*f/h* and *r/h*), are designed based on validated references to ensure consistency with previous findings. These parameters are illustrated in Figure 2 and quantitatively summarized in Table 1 [12]. This systematic variation enables a comprehensive evaluation of VG effects on the hydrodynamic behavior of the NACA 0021 hydrofoil in a VACT context.

Table 1 Single blade and VG specifications for numerical simulation

Part	Name/parameter	Specification/value
Single Blade in VACT	Hydrofoil type	NACA 0021
	Chord length (*c*)	0.14 m
	Span (*S*)	0.28 m
VGs	Shape	Rectangular, Trapezoidal
	Placement location (*x*)	10 %*c*, 15%*c*, 20 %*c*, 25 %*c*, 30 %*c*
	Configuration	single-row, contra-rotating
	Height *(h/c*)	δ
	Length (*l/h*)	3
	Angle (β)	18°
	Pair distance (*p/h*)	7
	Rear distance (*r/h*)	3.5
	Front distance (*f/h*)	1.65

Table 2 Main parameters of the small VGs simulated in this study

x / c (%)	*h* (mm)	*l* (mm)	*p* (mm)	*r* (mm)	*f* (mm)
10	0.38	1.14	2.66	1.33	0.63
15	0.49	1.47	3.43	1.72	0.81
20	0.60	1.80	4.20	2.10	0.99
25	0.72	2.16	5.04	2.52	1.19
30	0.87	2.61	6.09	3.05	1.44

In the numerical simulation of a foil with the addition of VGs, several variations are considered, including the dimensions and placement of the VGs, as shown in Table 2. The height of the VG changes for each difference in VG position relative to the *c*. This is because the VG height equals the BL thickness at each placement location on the foil surface. The relative height of VGs is typically represented by the variable h/δ, where *h* denotes the VG height and δ represents the boundary layer thickness [6, 27]. Based on their height, VGs are categorized into two types: conventional VGs ($h/\delta \geq 1$) and submerged VGs ($0.1 < h/\delta < 0.5$) [6], also known as "micro" or "low-profile" VGs. Every change in VG height always affects other VG dimensions, such as length (*l*), spacing between VG pairs (*p*), and the total number of VGs along the span for each variation of placement location (*x/c*).

Modifications in VG height inherently affect other geometric parameters, including the VG length (*l*), the spacing between counter-rotating VG pairs (*p*), and the total number of VGs distributed along the blade span for each placement variation (*x/c*). These interdependent dimensional changes are critical to maintaining the intended flow control characteristics, such as efficient vortex generation and sustained boundary layer attachment. Through systematic variation of these parameters, the simulation framework is designed to provide a robust evaluation of VG performance in mitigating flow separation, enhancing lift, and reducing drag on the NACA 0021 hydrofoil.

The BL thickness on a hydrofoil is determined using ANSYS Fluent by analyzing the velocity profile within the computational domain. The first step involves solving the flow field around the hydrofoil using either steady-state or transient simulations, depending on the nature of the problem [28]. Once the solution is obtained, the BL is identified by observing the velocity gradient near the hydrofoil surface, typically using the wall-function approach or a low-Reynolds number model [6]. Specifically, the BL thickness (δ) is defined as the distance from the surface at which the velocity reaches 99 % of the freestream velocity [29].

ANSYS Fluent calculates the BL characteristics by monitoring the velocity components in the vicinity of the hydrofoil surface. The BL thickness can be derived from the local velocity profiles using Fluent's post-processing tools [30]. Additionally, BL separation and transition can be analyzed by examining the change in the velocity gradients and flow direction near the hydrofoil surface, particularly in regions prone to flow separation and stall phenomena. Accurate determination of BL properties relies on a sufficiently refined mesh, especially near the hydrofoil surface, to resolve the velocity gradients effectively and capture the detailed behavior of the BL.

2.2 CFD Modelling

2.2.1 Computational domain

The computational domain was developed using ANSYS Design Modeler, with mesh generation conducted in ANSYS Meshing. To ensure fully developed flow and minimize boundary-induced effects, the domain was sized at 30*c*, consistent with best practices established in prior hydrodynamic studies [31]. As depicted in Figure 3, this domain configuration is optimized to facilitate α parameterization through the manipulation of inlet velocity components, thereby enabling the simulation of varying α without altering the hydrofoil's geometric orientation or creating multiple model instances [20].

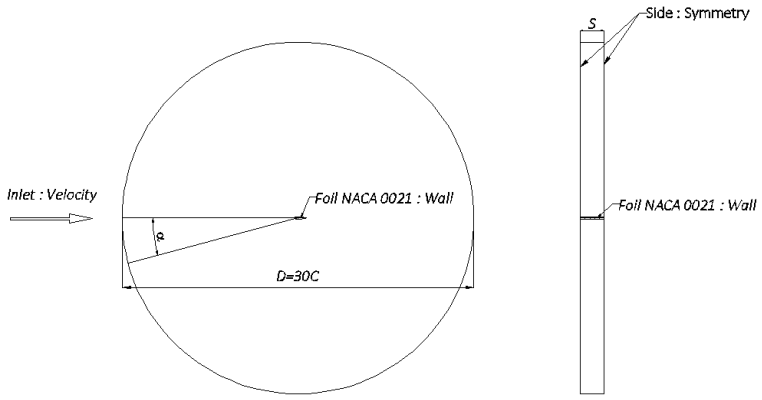

Fig. 3 Circular shape of the Computational domain and boundary conditions

This modeling strategy enhances computational efficiency while ensuring consistent boundary conditions across all cases. It further allows for a continuous sweep of α values, typically ranging from 0° to 180°, which is essential for accurately capturing the hydrodynamic response of the hydrofoil, particularly in the critical stall region. Such an approach is highly advantageous for evaluating unsteady flow phenomena and performance degradation due to flow separation.

The boundary conditions used during the numerical simulation were adjusted to match the test conditions conducted by Holst et al. [32]. The test conditions used air as the working fluid, on a Reynolds number of 1.8×10^5, a velocity of inlet 20 m/s, a turbulence intensity of 1 %, and a viscosity ratio of 6 [33]. Boundary conditions in the numerical simulation are adjusted to test conditions as shown in Figure 3. Side boundaries were set as symmetry to replicate the extended range used in further research. Hydrofoil surface and VG were set as no-slip wall boundary conditions. The low Reynolds number indicates that the hydrofoil may have difficulty in self-starting due to the lower fluid velocity.

The simulation campaign encompasses α ranging from 0 to 180°, using an incremental step of 5°. Particular emphasis is placed on the 0 to 40° range, which is recognized as the critical regime where stall onset and major hydrodynamic transitions typically occur. Focusing on this range enables a more refined analysis of the hydrofoil's hydrodynamic behavior, especially in relation to flow separation dynamics.

This selective approach provides deeper insights into how VGs influence lift enhancement, drag reduction, and stall mitigation under conditions where flow detachment is most prevalent. By isolating the performance characteristics within this critical α interval, the study can more effectively evaluate the

functional benefits of VG integration, informing optimal design parameters for improved hydrofoil and turbine blade efficiency in low to moderate angle regimes.

2.2.2 Meshing Generation and Setup

The computational domain is developed using ANSYS Design Modeler, and the meshing process is carried out in ANSYS Meshing. For the clean hydrofoil configuration, a hybrid O-type topology is adopted, with the domain radius set to 15 times the c to ensure far-field boundary effects are minimized. The mesh is composed of three distinct zones: a structured, multi-block region that accurately resolves the boundary layer; an unstructured zone surrounding the hydrofoil to maintain a relatively uniform cell size and improve flexibility; and a second structured region extending toward the far field to enhance numerical stability and grid quality.

The numerical simulation of CFD based on the RANS approach is commonly used to predict fluid flow behavior while efficiently accounting for turbulence effects. The RANS approach solves the time-averaged Navier–Stokes equations, where velocity fluctuations caused by turbulence are not directly simulated but are instead modeled using a turbulence model. RANS offers a balance between accuracy and computational efficiency. In this study, the k–ω *SST* turbulence model was employed. This model combines two turbulence models the k–ω (Wilcox) model and the k–ε model to take advantage of the strengths of each. Specifically, the k–ω model is applied near the wall region, as it can accurately predict velocity gradients and shear stress within thin boundary layers, while the k–ε model is used in the freestream region, as it is more stable and less sensitive to inlet boundary conditions [31].

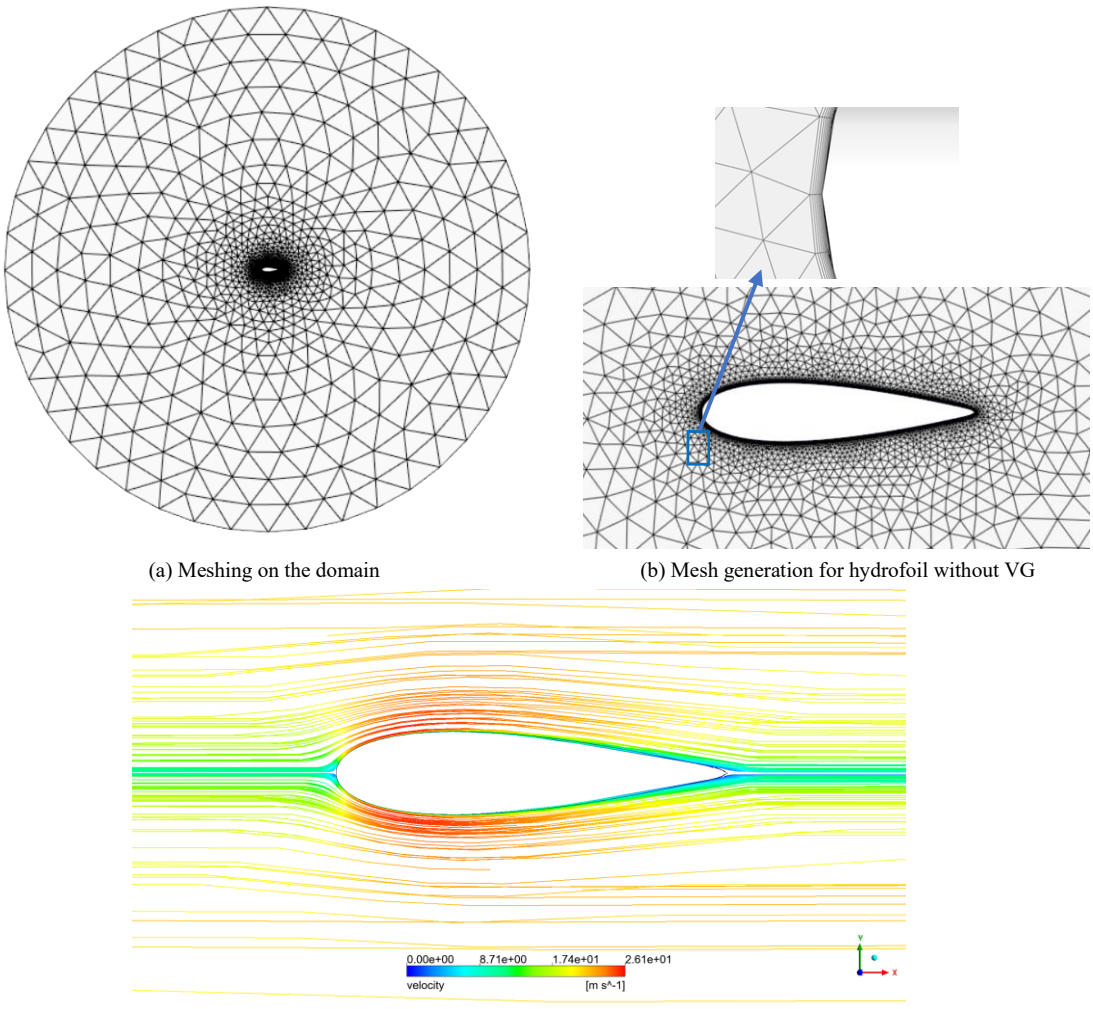

(a) Meshing on the domain

(b) Mesh generation for hydrofoil without VG

(c) Boundary layer

Fig. 4 Computational mesh for clean foil NACA 0021

The computational grid employed in this study for the baseline NACA 0021 hydrofoil consists of 1,467,736 elements and 405,280 nodes. The finest mesh density is concentrated near the hydrofoil surface to accurately resolve the near-wall flow characteristics, with a mesh growth rate of 1.2, as illustrated in Figure 4. The overall mesh distribution within the computational domain is presented in Figure 4(a), while a closer view of the mesh surrounding the hydrofoil is shown in Figure 4(b).

The CFD visualization in Figure 4(c) illustrates the development of the boundary layer along the surface of the hydrofoil, represented by color contours of velocity magnitude. The color variation clearly indicates the progressive change in flow velocity from the free-stream region to the near-wall zone. In the region close to the leading edge, the velocity gradient near the wall is relatively steep, signifying a thin boundary layer and strong wall shear. As the flow moves downstream, the boundary layer thickens gradually due to viscous effects and momentum loss near the wall. This thickening is evident from the expansion of the low-velocity region (dark blue) adjacent to the surface.

In this study, a specific y^+ value of 0.85 has been included to ensure adequate near-wall resolution and to improve the accuracy of the boundary layer representation. Maintaining y^+ below 1 in the near-wall region ensures accurate resolution of the viscous sublayer, consistent with the requirements of the *k–ω SST* turbulence model. This approach enables a wall-resolved simulation, allowing the near-wall flow behavior to be captured without the use of wall functions, thereby improving the accuracy of shear stress and pressure distribution predictions along the hydrofoil surface. The computational grid near the wall region was refined using a first inflation layer height of 1.2981×10^{-5} m to achieve the desired y^+ value, with a growth rate of 1.2 and layers number of 9 to maintain mesh quality and numerical stability. This mesh configuration ensures that the development, separation, and reattachment of the boundary layer are accurately resolved, which is essential for evaluating the hydrodynamic performance of the hydrofoil equipped with micro-VGs.

Mesh quality refers to the measure of how well the elements in a mesh align with ideal geometric properties to ensure accurate and efficient simulations. High-quality meshes minimize numerical errors, improve solution stability, and enhance computational efficiency. The mesh quality summarized in Table 3 shows that the skewness value is below 0.25, indicating good quality; the orthogonal quality is below 0.8; and the aspect ratio lies within the acceptable range of 5-8.

Table 3 Mesh Quality

Quality	Hydrofoil NACA-0021
Skewness	0.2168
Orthogonal Quality	0.7813
Aspect Ratio	5.7708

Secondly, the meshing was generated for the NACA 0021 hydrofoil model with the addition of VGs, where the VG height was set equal to the local boundary layer thickness. The boundary layer thickness varies along the *x/c* position, being thinner near the leading edge and gradually increasing toward the trailing edge, as shown in Table 2. To maintain consistency, the meshing approach used for the original hydrofoil is adopted for meshing the hydrofoil with VGs.

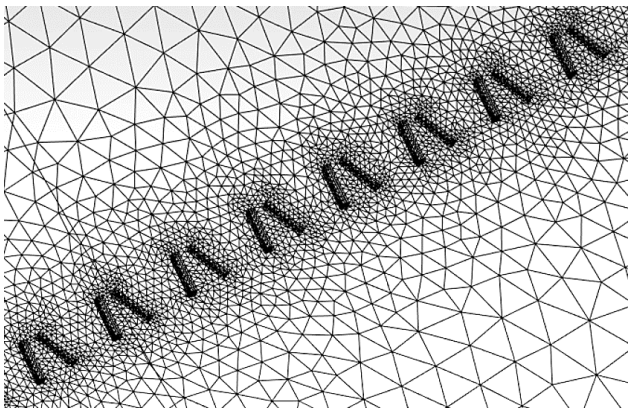

Fig. 5 Mesh generation for the foil with integrated VG

Figure 5 illustrates one of several VG placement variations on the foil surface in this study, consisting of a single row with a contra-rotating configuration, where the VGs are arranged along the span. The total number of mesh elements used is 3,692,602 elements, and the node number is 916,662 nodes. The VG meshing is constructed with a density level of 10 % of the VG height.

2.2.3 Numerical Setup

URANS solves the RANS equations while accounting for unsteady behavior in the flow that evolves over time. Although turbulence is still modeled through time-averaged equations, URANS is capable of capturing significant transient phenomena such as periodic vortex shedding, transient stall, fluctuating hydrodynamic forces on hydrofoils, and non-stationary vortex interactions. This approach requires time-step computations, which results in higher computational costs compared to steady RANS, but provides a more realistic representation of physical flow behavior.

In RANS, the flow is assumed to be in a steady-state condition where flow parameters such as velocity, pressure, and aerodynamic forces do not change with time. Although the real flow is inherently turbulent and fluctuating, the effect of turbulence is represented through time-averaged values, eliminating the need for time-dependent calculations. This method is computationally efficient and is suitable for studies focused on steady-flow conditions, without requiring predictions of time-varying phenomena such as force oscillations, vortex shedding, or unsteady stall dynamics. Since modeling detailed VG geometries demands fine mesh resolution and significant computational effort, most numerical studies have instead implemented simplified VG models to achieve a balance between accuracy and efficiency [3].

This turbulence model has been formulated using *k-ω SST* [18], which is known for its excellent performance and accuracy in adverse pressure gradients and separated flows. In the present simulations, a low-Reynolds-number approach without wall functions was adopted, allowing the near-wall flow to be resolved directly down to the viscous sublayer. Consequently, the near-wall mesh was designed to satisfy a dimensionless wall distance of $y^+<1$, ensuring adequate resolution of the boundary layer.

2.2.4 Verification and validation

Validation is a crucial step in the CFD workflow, ensuring the accuracy of results by comparing them with experimental reference data. Quality assurance plays an essential role in ensuring that CFD results are of high quality, reproducible, and traceable [20, 32, 34]. It establishes standardized procedures and verification protocols that help minimize numerical errors and inconsistencies. Sensitivity analysis aims to assess the impact of various parameters, by providing a consistent methodological approach to achieving accurate numerical results, particularly for thick current turbine hydrofoils. This approach is essential for understanding how small variations in design parameters or boundary conditions can influence flow characteristics and hydrodynamic performance. The following sections elaborate on these topics, beginning with the analysis of the clean profile and subsequently transitioning to the controlled profile.

In the CFD simulations performed using ANSYS Fluent, the Finite Volume Method (FVM) is employed, in which the governing conservation equations are discretized and solved over individual control volumes. Consequently, grid resolution in the grid-dependence study is more appropriately characterized by the number of control volumes rather than by the number of nodes or geometric mesh elements. As demonstrated by the results obtained for progressively refined grids, variations in the C_L and C_D directly reflect the influence of control-volume resolution on discretization errors. This approach is consistent with the fundamental principles of FVM, where numerical accuracy and solution convergence are governed by the size and distribution of the control volumes within the computational domain. Accordingly, the evaluation of the Grid Dependence (GD) Index and the Grid Convergence Index (*GCI*) based on control-volume counts provides a more rigorous basis for assessing numerical accuracy and for ensuring that the computed solutions systematically approach the grid-dependence limit.

Grid dependence refers to the sensitivity of CFD results to spatial discretization, as numerical solutions obtained using the Finite Volume Method (FVM) inherently contain discretization errors that depend on the size, distribution, and number of control volumes. A grid-dependence study is therefore performed through

systematic grid refinement to evaluate whether key solution variables asymptotically approach a grid-independent solution as the mesh is refined [35, 36].

Table 4 Grid dependence test (GDT)

Elements	C_D	*GI*	C_L	*GI*
365,782	0.0356408	-	0.5978161	-
733,522	0.0351602	0.032	0.6026012	0.022
1,467,736	0.0354005	0.019	0.6118848	0.043
2,935,503	0.0356692	0.060	0.6145331	0.013

A grid dependence study was carried out on the hydrofoil model without VG at an α of 10°. The resulting C_L and C_D from the simulation were validated against the experimental data of Holst et al. [32]. A grid dependence test was performed using the coupled second-order upwind method to evaluate the *GD* values for C_L and C_D across varying element counts: coarse (733,522 elements), medium (1,467,736 elements), and fine (2,935,503 elements). The findings of this study elucidate the influence of elements count variations on the measured values of C_L and C_D. The GDT conducted between the medium and fine grids yielded results of 1.9 % for C_D and 4.3 % for C_L.

The *GCI* is a standardized quantitative metric used to estimate the numerical uncertainty arising from grid discretization in CFD simulations. Originally introduced by Roache [31], the *GCI* provides a systematic framework to assess the proximity of a numerical solution to the grid-independent (asymptotic) solution through comparisons of results obtained on successively refined grids [37]. The method is based on Richardson extrapolation, which assumes that numerical solutions converge toward the exact solution at a predictable rate as the grid is refined [35]. By performing simulations on at least three systematically refined grids, the apparent order of accuracy and discretization error can be estimated, allowing the *GCI* to be expressed as a conservative percentage measure of the relative discretization uncertainty [37]. A smaller *GCI* indicates weak sensitivity to further grid refinement and low numerical uncertainty, whereas a larger *GCI* suggests strong grid dependence and the need for additional refinement. Owing to its transparency and reproducibility, the *GCI* methodology is widely recommended in CFD best-practice guidelines for reporting numerical accuracy independently of experimental validation [37].

The order of convergence, denoted as *p*, is estimated to evaluate the rate at which the numerical solution converges as the grid is refined. It is calculated using the solutions obtained from successive grid levels and reflects the effectiveness of the numerical scheme in reducing discretization error. A *p* value approaching the formal order of accuracy of the numerical method indicates regular convergence behavior, whereas deviations from the expected order may suggest nonlinear effects or remaining numerical errors.

$$p = \frac{\ln\left|\frac{\varepsilon_{32}}{\varepsilon_{21}}\right|}{\ln(r)} \tag{1}$$

Richardson extrapolation is used to estimate the solution on an infinitely fine grid:

$$\phi_{ext} = \phi_1 + \frac{\phi_1 - \phi_2}{r^p - 1} \tag{2}$$

The *GCI* is calculated using the difference between solutions on refined grids, the grid refinement ratio, and the estimated order of convergence. A safety factor (*Fs*) is applied to provide a conservative estimate of numerical uncertainty, which is expressed as a percentage and used to assess the sensitivity of the solution to grid resolution. *Fs* = 1.25 is the safety factor recommended by Roache. A small *GCI* value indicates weak dependence of the numerical solution on grid resolution, whereas a large *GCI* value reflects significant sensitivity to grid refinement and non-negligible discretization errors. Formula of the *GCI*:

For the medium $_2$ - coarse $_1$ grid pair:

$$GCI_{21} = F_s \frac{|\phi_1 - \phi_2|}{|\phi_1|(r^p - 1)} \times 100\ \% \tag{3}$$

For the fine $_3$ - medium $_2$ grid pair:

$$GCI_{32} = F_s \frac{|\phi_2 - \phi_3|}{|\phi_2|(r^p - 1)} \times 100\ \% \tag{4}$$

Asymptotic range verification was conducted to confirm that the numerical solution converges in a systematic manner with grid refinement. The agreement between the *GCI* ratios and the grid refinement ratio indicates that the solution lies within the asymptotic convergence range, and the associated numerical uncertainty can therefore be considered reliable. The simulation is within the asymptotic convergence range. If this condition is satisfied, the simulation is within the asymptotic convergence range, and the *GCI* assessment is mathematically valid.

$$\frac{GCI_{32}}{GCI_{21}} \approx r^p \tag{5}$$

Table 5 Grid Convergence Index (GCI)

Elements Number	C_D	*GCI*	C_L	*GCI*
365,782	0.0356408		0.5978161	
733,522	0.0351602	-0.0135	0.6026012	0.0109356
1,467,736	0.0354005	0.009276	0.6118848	0.0112489
2,935,503	0.0356692		0.6145331	

Table 5 presents the GCI results for various mesh sizes: coarse, medium, fine, and very fine. Grids with the number of elements ranging from 1,467,738 to 2,935,503 elements obtained the lowest *GCI* values. The *GCI* values of 0.928 % for the C_D and 1.125 % for the C_L indicate low numerical uncertainty due to grid discretization. These results suggest that further mesh refinement would lead to only marginal changes in the computed aerodynamic coefficients, and the solution can therefore be regarded as nearly grid-dependence.

In general, research on hydrofoil performance, particularly for aircraft or horizontal axis turbines, is more intensively conducted within the α range of 0-30°, as this is considered a critical stall region. However, when the hydrofoil is applied to a vertical-axis turbine, the incidental α of the hydrofoil becomes significantly wider. Experimental data by Holst et al. [32], and numerical by Sheldahl and Klimas [34], and Satrio et al. [20] provide a more comprehensive α range (0-180°) for the NACA 0021 foil, making it a key reference case for this study. The experiments conducted by Holst et al. [32] were performed in a wind tunnel. Fortunately, a Reynolds number (*Re*) of 1.8×10^5 is relatively easy to replicate with an appropriate inflow velocity. The force response does not exhibit significant variations across different working fluids (air and water) as long as they are conditioned at the same *Re* [20, 32, 34].

The simulation results exhibit trends consistent with reference data. As shown in Figure 6(a), C_L from the simulation increases steadily with the α from 0° to 15°, before stalling at α = 20°. Beyond this point, C_L begins to decrease, although the decline is less abrupt than in the reference case. Up to α = 90°, the simulation tends to over-predict C_L values, momentarily aligning with the reference before underpredicting in the range of α = 110° to 150°. Within this range, the hydrofoil simulation revealed the shedding of large-scale flow structures, resulting in a complex flow field that was challenging to capture accurately.

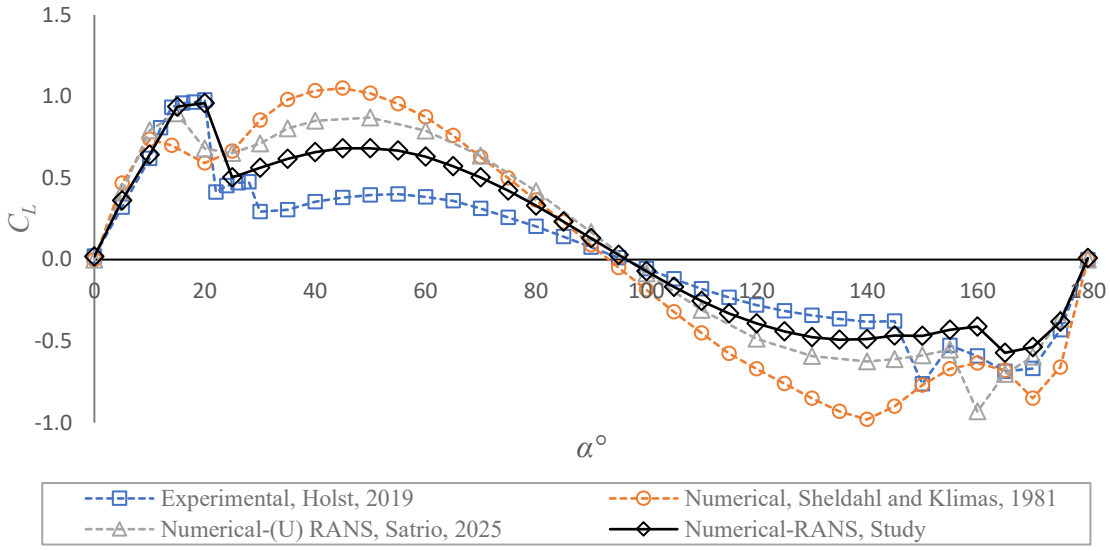

(a)

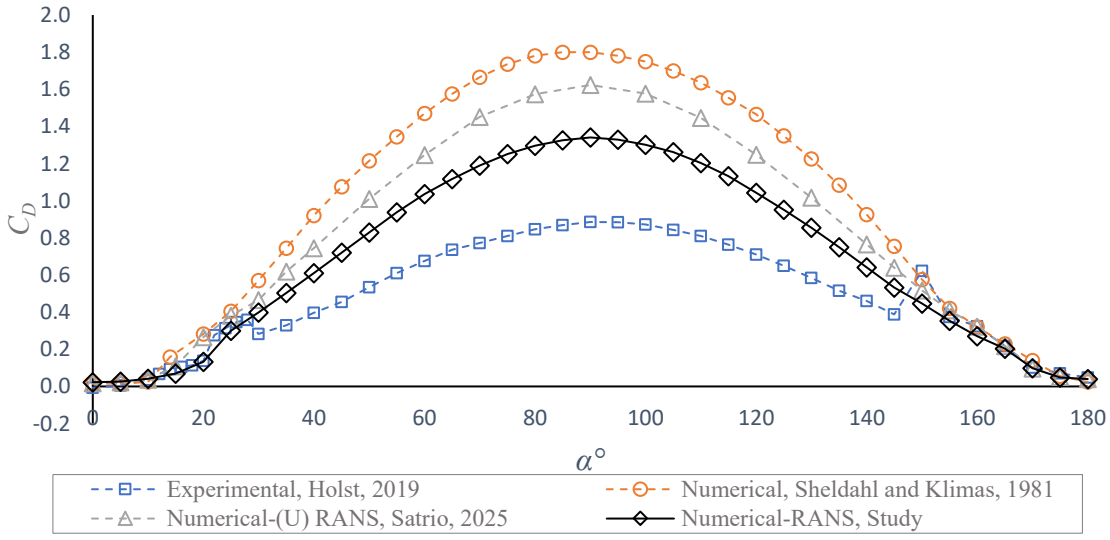

(b)

Fig. 6 Numerical variations of (a) C_L and (b) C_D

Figure 6. illustrates the relationship between C_L and C_D as a function of the α. The data include both experimental measurements and numerical simulation results obtained from previous studies. This validation focuses on the NACA 0021 hydrofoil operating at a Reynolds number of 1.8×10^5, aiming to verify the accuracy and reliability of the present numerical approach.

A comparison between experimental data by Holst [33] and data by Sheldahl and Klimas [34] numerical simulation approach shows striking differences. This is then compared with data from Satrio [20] numerical simulation approach and data from this study, as shown in Figure 6(a). Figure 6(a) illustrates that C_L remains consistent within the α range of 0-20°, corresponding to the initial stall region. A similar trend is observed at α = 70-110° and α = 170-180°. According to the data reported by Holst, 2019, the second stall occurs at α = 30°. Furthermore, within the ranges of α = 30-70° and α = 110-170°, a significant discrepancy between the two datasets can be observed.

Figure 6(b) shows that C_D remains consistent within the ranges of α = 0-30° and α = 150-180°, while a pronounced difference is evident in the intermediate range of α = 30-150°. These inconsistencies may introduce bias if the experimental data are used directly for validation. Comparing the experimental C_D data by Holst et al. [32] with the data from Sheldahl and Klimas [34] numerical approach shows a difference of up

to 47.4 %. The numerical C_D results based on URANS by Satrio, 2025 and Holst, 2019 show a deviation of up to 26 %, with a difference of 10.3 % compared to Sheldahl, 1981. However, in this study, the C_D values obtained from the numerical simulation based on RANS differed by approximately 26.9 % from the experimental data by Sheldahl and Klimas [34] and Holst [33], while the difference with Satrio et al. [20] was smaller at 11.4 %.

To achieve a more consistent comparison, the present study performs a numerical validation against the results obtained by Satrio et al. [20], 2025, who employed an URANS method with the *k–ω SST* turbulence model at the same Reynolds number of 1.8×10^5, as shown in the Figure 6. The difference between the RANS and URANS results is relatively small. The slight deviation observed in the RANS simulation can be attributed to minor variations in the solver setup and mesh configuration. Overall, the close agreement between the two numerical approaches confirms that the present CFD model provides sufficient accuracy and reliability for the hydrodynamic analysis of the NACA 0021 hydrofoil [19].

Figure 6 presents the C_D obtained in this study alongside the experimental data. The results indicate that the simulation accurately predicted C_D within the α range of 0-25° and 50-180°. Additionally, several numerical studies have reported that simulation results closely follow the experimental trend in the pre-stall regime.

3. Result and Discussion

The Mean Absolute Percentage Error (MAPE) equation was used to compare the results of this study with those of other researchers. Since this method considers all data points within the numerical range (0-180°), which covers a total of 27 angle-of-attack variations. The results indicate an error of 7.75 % for C_L and 20.47 % for C_D when compared with the experimental data reported by Holst et al. [32]. In comparison with the numerical approach results of Sheldahl and Klimas [34], the errors were 6.0 % for C_L and 26.9 % for C_D, while relative to the URANS-based simulation by Satrio et al. [20], the errors were 1.3 % for C_L and 11.4 % for C_D. These findings indicate that the results of this study are better than those of the other two researchers, as they provide a better fit for the experimental data.

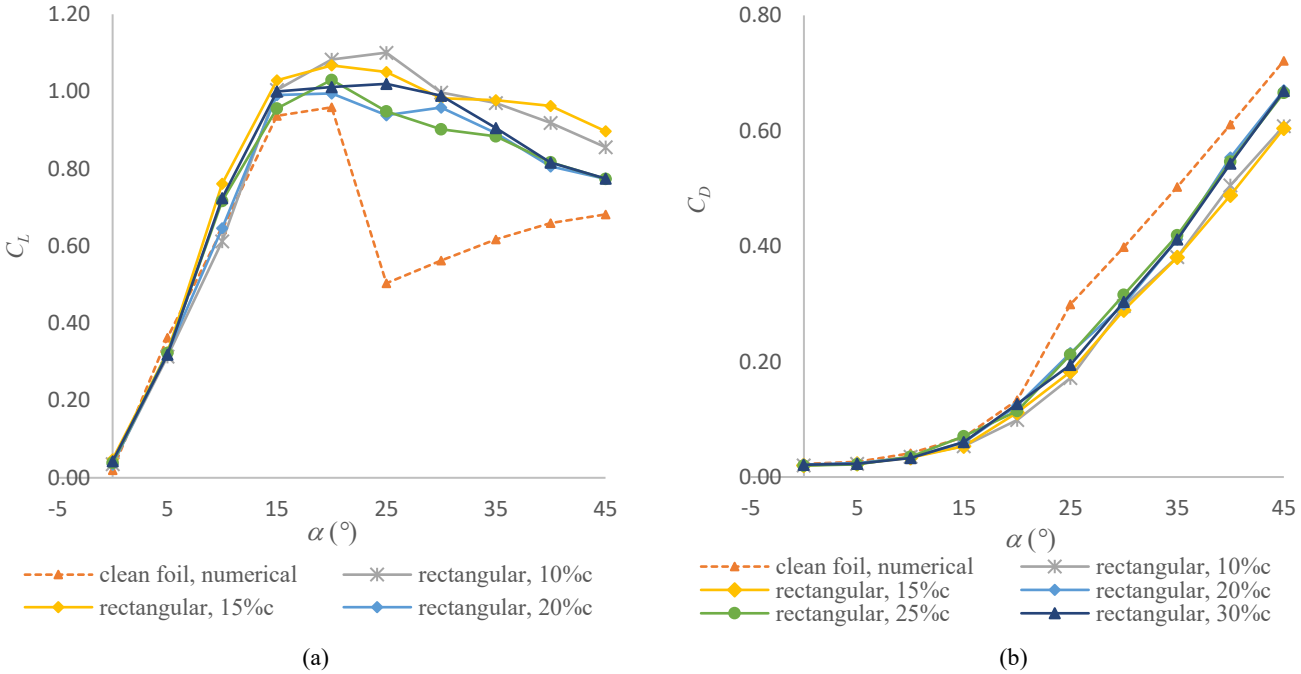

(a) (b)

Fig. 7 Numerical variations of (a) C_L, and (b) C_D in the α range of 0-45° on foil with rectangular VG

The numerical simulation results for the NACA 0021 foil with rectangular VGs arranged in a single row at different positions along the chord length (10-30 %*c*). The VG height (*h*) was set equal to the boundary layer thickness (δ) at each respective location. The simulation results demonstrate that the peak lift coefficient increased with the addition of VGs, with the most significant lift enhancement occurring at the 10 %*c* position,

followed by the 15 %*c* position, shown as Figure 7(a). This finding indicates that positioning the VGs closer to the leading edge leads to the highest improvement of the lift [12]. Meanwhile, Figure 7(b) presents the numerical simulation results for the C_D. The results show that the addition of VGs reduces drag and increases lift, thereby enhancing overall turbine performance.

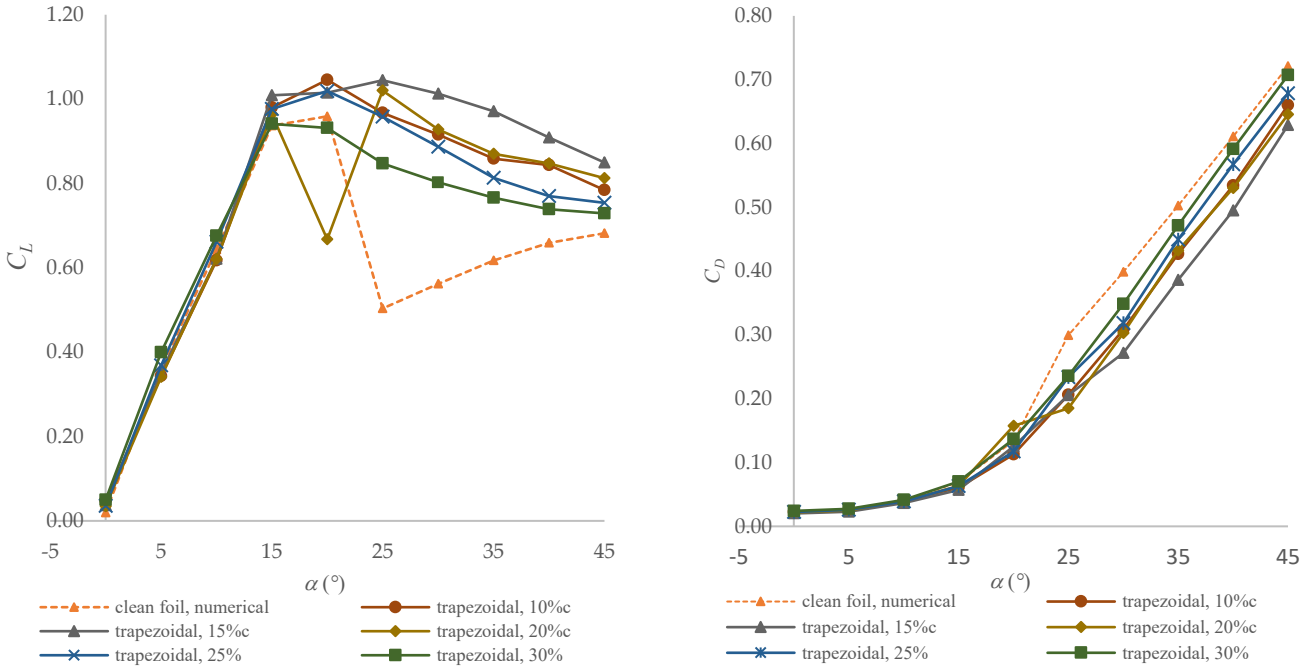

(a) (b)

Fig. 8 Numerical variations of (a) C_L, and (b) C_D in the α range of 0-45° on foil with trapezoidal VG

Figure 8(a) illustrates the numerical simulation results for the hydrofoil fitted with trapezoidal VGs. The data reveals that the highest C_L is achieved at an α of 20°, with VGs placed at 10 %*c*, followed by the 15 %*c* position. These results indicate that locating VGs closer to the leading edge significantly enhances lift performance. Figure 8(b) shows that the minimum C_D occurs within the α range of 15 to 25°, with the most notable reduction at the 10 %*c* position, followed by the 15 %*c* position. Compared to the baseline hydrofoil without VGs, these configurations demonstrate improved hydrodynamic efficiency.

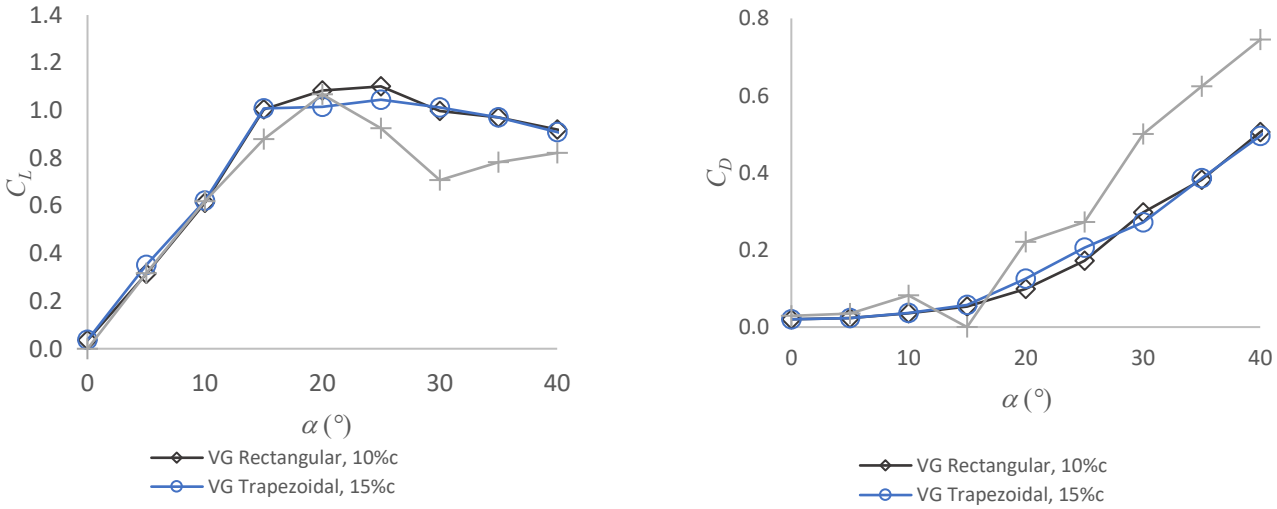

(a) (b)

Fig. 9 Numerical results of the blade with vortex generators: (a) C_L and (b) C_D versus α

Research on the addition of VG to the NACA 0021 foil blade is still very limited. Due to this limitation, we refer to previous studies conducted by other researchers using a numerical approach. As shown in Figure

9. a, Satrio et al. [20] used the URANS method and the same *k-ω SST* turbulence model, the geometry of the NACA 0021 blade, the triangular VG shape. The numerical results of Satrio's research show an increase in α = 20°, then show a decrease in the C_L at α up to 25°. The same thing happens to rectangular and trapezoidal VGs, but the increase reaches α = 25°. Meanwhile, Figure 9.b shows that the C_D value for the triangular VG exceeds the value of the hydrofoil without VG, while for the square and trapezoidal VGs the C_D is lower than the C_D of the hydrofoil without VG. This is because in the simulation the dimensions of the triangular VG are larger than the dimensions of the square and trapezoidal VGs.

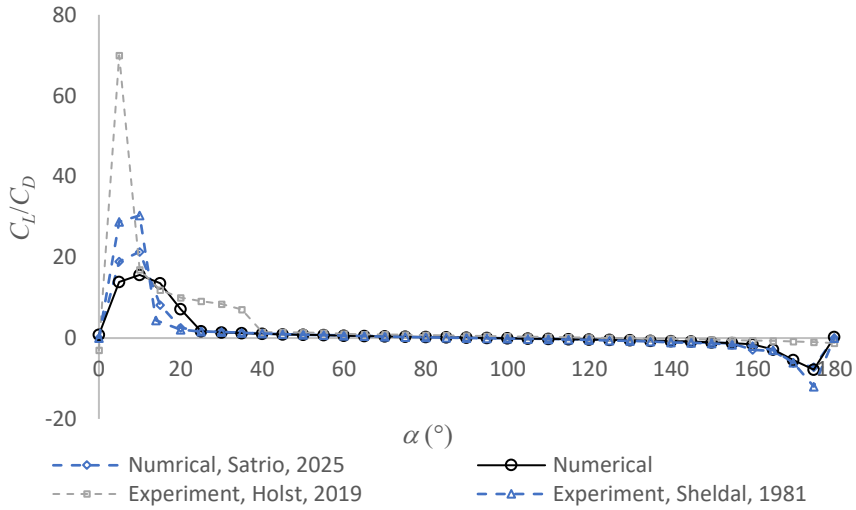

Fig. 10 The correlation between the C_L/C_D ratio and the α, NACA0021

For a hydrofoil without VGs, the lift-to-drag ratio (C_L/C_D) is recorded at 13.62 when operating at α = 15° but drops to 7.18 at α = 20°. The addition of rectangular VGs positioned at 10 % of the chord length significantly enhances hydrodynamic efficiency, increasing the C_L/C_D to 19.29 at α = 15° and to 9.55 at α = 20°. Similarly, trapezoidal VGs installed at 15 % of the chord length also contribute to performance improvement, resulting in a C_L/C_D of 17.64 at α = 15° and 8.09 at α = 20°.

Figure 10 presents a comparison of the C_L/C_D with varying α, based on numerical and experimental data obtained by each researcher. The figure shows a striking difference between the experimental results of Holst, 2019 and the numerical results of Sheldahl and Klimas [34], with the most significant difference occurring at angles between 5 and 10°. However, the numerical results of this study and Satrio et al. [20] and this study show closer agreement and similar trends with the numerical data reported by Sheldahl and Klimas [34].

Elevated C_L/C_D values correspond to superior hydrodynamic performance by maximizing lift while minimizing drag, whereas diminished ratios reflect increased drag penalties that impair efficiency. This hydrodynamic parameter is contingent upon several variables, including hydrofoil geometry, α, flow conditions, and surface modifications such as VGs. Implementing VGs is a strategic intervention aimed at augmenting lift and mitigating drag, thereby refining the C_L/C_D for optimal hydrodynamic functionality [35].

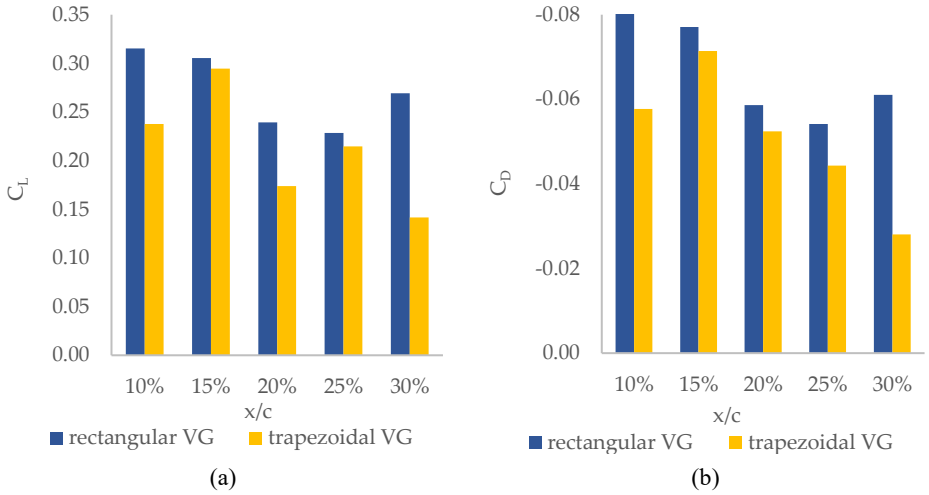

Fig. 11 Average increase in lift (a) and the reduction in drag (b) from different VG shapes

Figure 11 presents the average increase in C_L and the corresponding decrease in drag for each VG configuration, using both rectangular and trapezoidal shapes. The analysis was conducted over a geometry, α ranges from 15 to 40°, which represents a critical region where hydrodynamic performance is highly sensitive to flow changes.

As shown in Figure 11(a), the highest average C_L improvement was observed with rectangular VGs placed at 10 %c, achieving an average C_L increase of 0.315. Trapezoidal VGs positioned at 15 %c also demonstrated a significant improvement, with an average C_L increase of 0.295. A similar trend is evident in Figure 11(b), where the greatest average reduction in C_D occurred with rectangular VGs at 10 %c, resulting in an average C_D reduction of 0.08, while trapezoidal VGs at 15 %c achieved a reduction of 0.071. However, the hydrofoil without VGs produced an average C_L of 0.72 and an average C_D of 0.28.

These results indicate that the placement and geometry of VGs play a crucial role in modifying the boundary layer characteristics, thereby enhancing hydrodynamic performance [38]. Specifically, the optimal positioning of rectangular VGs at 10 %c appears to generate stronger streamwise vortices, which delay flow separation more effectively and contribute to both increased lift and reduced drag. The slightly lower, yet still substantial, performance of trapezoidal VGs at 15 %c suggests that their geometry and position also facilitate beneficial flow control, though to a lesser extent. Overall, the findings highlight the importance of careful VG configuration to maximize hydrodynamic efficiency [36].

3.1 Velocity field and Pressure distribution

Figure 12 presents the time-averaged streamlines colored by the velocity magnitude distribution on the midspan plane for various α, comparing hydrofoil configurations without and with VGs of rectangular and trapezoidal shapes. The velocity contour patterns provide insights into the locations of flow separation and stall phenomena. As the α increases, the separation point on the suction side tends to shift closer to the leading edge. As previously discussed, the implementation of VGs on the hydrofoil helps delay stall to higher α, thereby enhancing the overall performance of the turbine blades.

Figure 12 illustrates the streamlines colored by the velocity magnitude distributions at various α for the hydrofoil configurations without and with VGs. The NACA 0021 hydrofoil was modified by adding rectangular-shaped VGs with a height of $h=\delta$, where δ represents the boundary layer thickness at the 25 %c location. These VGs were positioned at 10 %c from the leading edge.

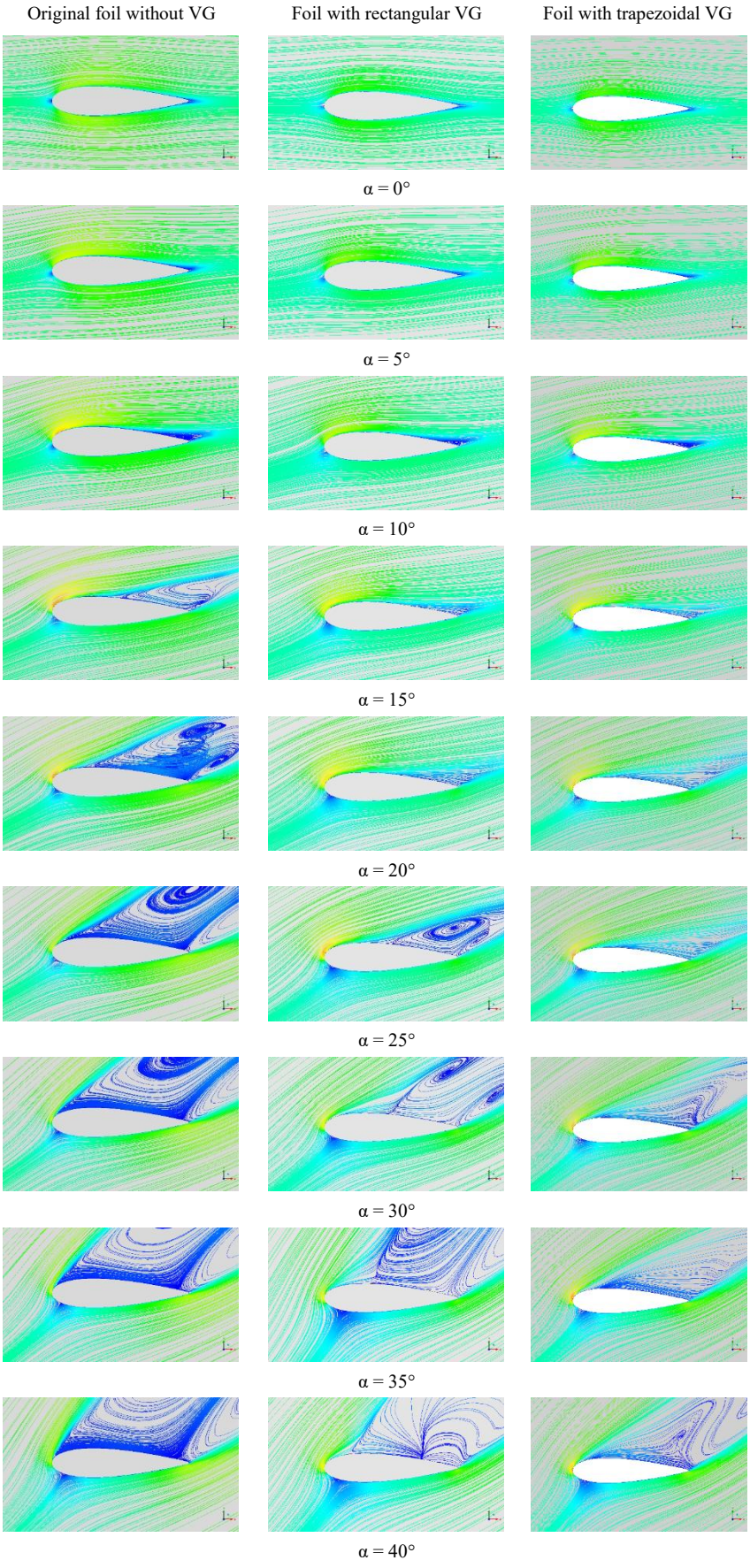
Original foil without VG
Foil with rectangular VG
Foil with trapezoidal VG
α = 0°
α = 5°
α = 10°
α = 15°
α = 20°
α = 25°
α = 30°
α = 35°
α = 40°

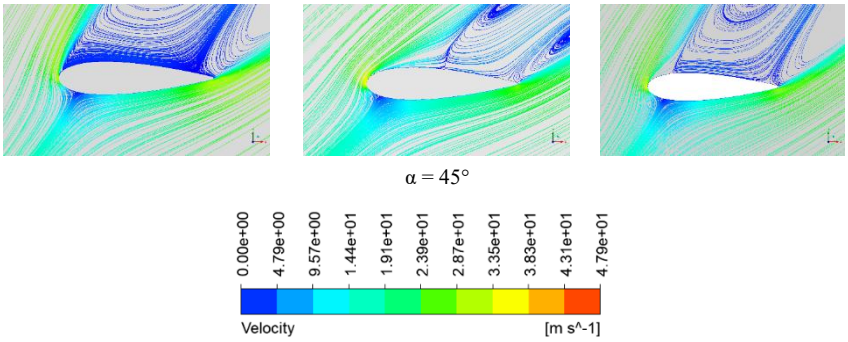

Fig. 12 Streamlines colored by the velocity magnitude are compared at different α for the baseline hydrofoil and those with rectangular and trapezoidal VGs

A comparative analysis of the streamlines colored by the velocity magnitude for the hydrofoil with and without VGs is presented below.

- It is clearly observed that from an α of 0 to 10°, no significant flow separation occurs in any of the variations, as indicated by the similar velocity distribution patterns [38]. From the left side of the figure, the clean hydrofoil (without VGs) progressively stalls beyond 20°. As the α increases, the recirculation zone expands accordingly. The effects of the vortex generators are immediately evident: the low-velocity regions are significantly reduced at all α, and the wake remains more stable and aligned with the trailing edge direction.
- The impact of flow separation, characterized by a reduction in the high-velocity flow area, is most pronounced within the α = 20-25° range. Within this range, the configuration without VGs exhibits a larger low-velocity region, marked in blue, indicating significant flow separation. This velocity reduction leads to energy loss, resulting in decreased lift and increased drag, ultimately reducing the overall efficiency of the turbine blade.
- The velocity phenomena observed on the hydrofoil without VGs at α between 25 and 45° are largely influenced by flow separation and stall, with the low-velocity region (shown in blue) extending all the way to the leading edge. In contrast, for the hydrofoil equipped with VGs, flow separation reaching the leading edge occurs only at higher α, between 35 and 45°, while at 25 to 30°, the low-velocity region is confined between 30 and 40 %c. The VG configurations with height $h = \delta$ effectively delay flow separation by re-energizing the boundary layer, shifting the separation points to 30 and 40 %c, respectively. Additionally, higher velocity flow is observed near the upper surface of the hydrofoil in both VG configurations, as indicated by the green color.

The range of α examined spans from 0 to 20°, with the C_L exhibiting a linear increase up to the onset of stall. For the clean hydrofoil configuration, the stall typically occurs at approximately 12° [23], while for the hydrofoil equipped with VGs, it occurs around 18-20°, as reported in [24]. Flow separation phenomena begin to emerge, leading to a degradation in C_L performance.

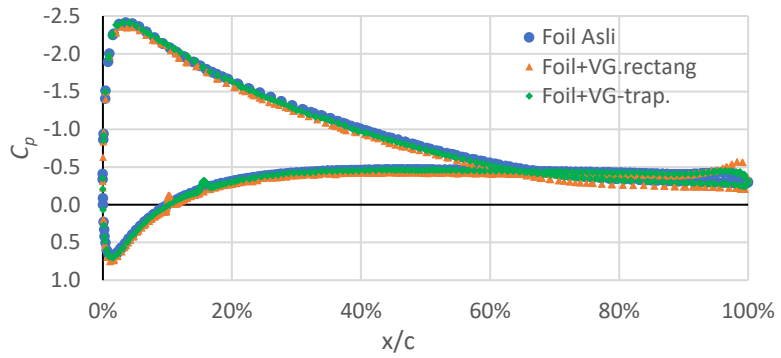

(a)

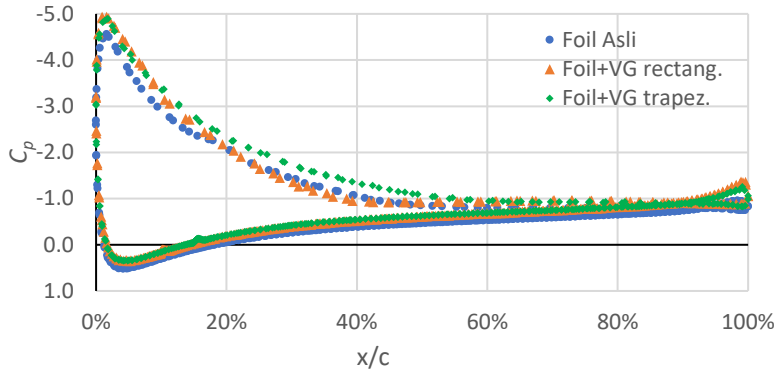

(b)

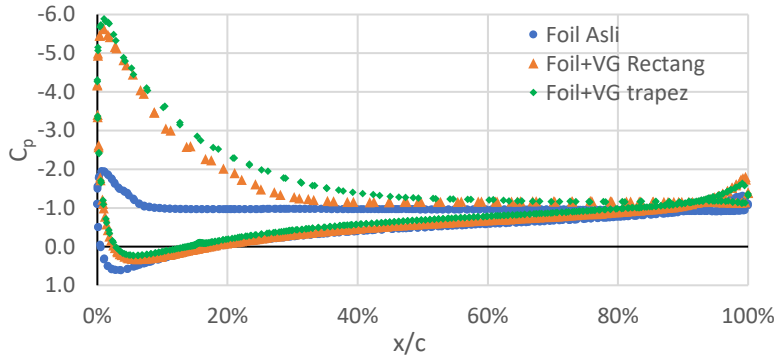

(c)

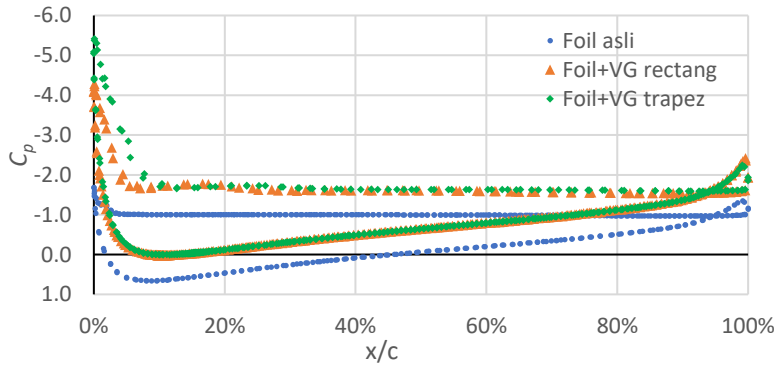

(d)

Fig. 13 Comparison of the pressure coefficient distribution on an hydrofoil without and with VGs, (a) $\alpha = 10°$, (b) $\alpha = 20°$, (c) $\alpha = 25°$, and (d) $\alpha = 40°$

Figure 13(a) presents the pressure coefficient (C_p) distribution at an $\alpha = 10°$ for the simulated hydrofoil models without and with VGs of different square and trapezoidal shapes. The selection of $\alpha = 10°$ is based on

the observation that within the range of $\alpha = 0°$ to $\alpha = 10°$, there is no significant difference in the C_L and C_D, as illustrated in Figure 12 [39]. The shape of the pressure coefficient curves is relatively similar among the hydrofoil without VG and those equipped with VGs of different geometries. The leading section of the hydrofoil exhibits higher pressure and lower flow velocity, resulting in a high-pressure region due to fluid compression. Figure 13(b) illustrates that at $\alpha = 20°$, the C_p on the leading side of the hydrofoil with VGs increases beyond that of the hydrofoil without VGs. This enhancement contributes to the observed increase in C_L and reduction in C_D. Figure 13(b) illustrates the range of $\alpha = 15°$ to $\alpha = 20°$, the C_p on the leading side of the hydrofoil with VGs increases beyond that of the hydrofoil without VGs. This increase contributes to the improvement in C_L and the reduction in C_D. The curves indicate that Figures 13(c) and 13(d), which represent the conditions at $\alpha = 25°$ to $\alpha = 40°$, show a significant pressure drop on the suction side (face side) of the hydrofoil with VGs, while the hydrofoil without VGs exhibits a relatively higher pressure in this region.

As depicted in the C_p curves in Figure 13, a noticeable shift occurs from $\alpha = 20°$ to $\alpha = 40°$, where the pressure distribution on the rear surface of the foil experiences a substantial decrease. Conversely, the pressure on the front surface (face side) of the hydrofoil increases considerably. Among the VG configurations, the square-shaped VG demonstrates superior hydrodynamic performance compared to the trapezoidal-shaped VG.

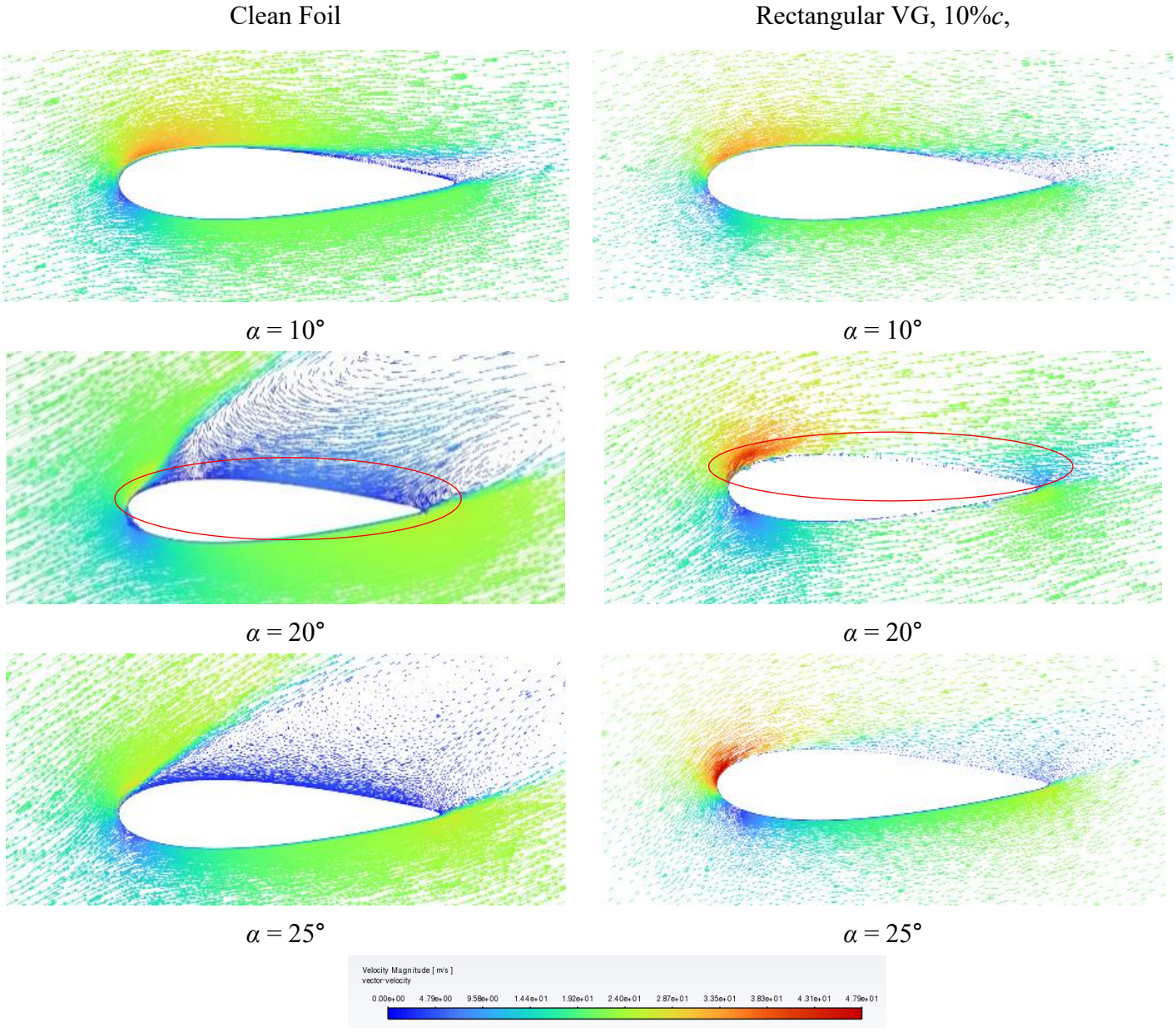

Fig. 14 Flow separation on the hydrofoil without and with VGs

3.2 Flow Separation

Figure 14 presents the flow separation conditions at α ranging from 10 to 25°. At α = 10°, the flow separation points observed on the NACA 0021 hydrofoil, both with and without vortex generators, shows a similar separation pattern. The flow separation point occurs at 75 %*c* for both the foil without and with additional VG.

The $\alpha = 20°$ represents the critical angle at which the NACA 0021 hydrofoil experiences stall. As shown in Figure 14, at $\alpha = 20°$, a hydrofoil without a VG experiences significant flow separation, with the separation point at 70 % of the chord length and then stalls with further increases in the angle. At $\alpha = 20°$, a hydrofoil with a VG exhibits a slightly different trend, with the flow separation point at approximately 65 %*c*, suggesting that the addition of a VG contributes to delaying stall.

At an $\alpha = 25°$, the flow separation point on a hydrofoil without a vortex generator extends from the leading edge to the trailing edge, ultimately causing stall. In contrast, the hydrofoil equipped with vortex generators is still able to withstand flow separation. The square-type VG exhibits flow separation up to approximately 50 % of the chord length. This finding indicates that the geometry and placement of the vortex generators significantly influence the formation of vortices responsible for delaying stall. Therefore, the VG geometry and its placement on the hydrofoil surface play a crucial role in achieving maximum stall delay.

The delay in stall leads to an increase in the C_L and a reduction in the C_D. Consequently, the combined effect of higher C_L and lower C_D enhances the overall efficiency of the turbine.

3.3 Prediction of Turbine Power Enhancement by Integrating Vortex Generators (VGs)

The integration of a VG on the blades of a VACT, based on simulation data and simplified analytical considerations, requires several underlying assumptions. This approach is intended solely to obtain a preliminary prediction of the impact of VG integration on the VACT's performance. In general, achieving more accurate predictions requires further simulations involving the entire rotating turbine to comprehensively explore its overall behavior.

Figure 14 shows the change in a single blade's speed vector over a single rotation. Even with constant rotating speed and current speed, the resultant velocity and α vary in both direction and amplitude with azimuth angle. The upstream half-cycle ($0° < \theta < 180°$) of the bar is positive, whereas the downstream half-cycle ($180° < \theta < 360°$) is negative.

The hydrodynamic performance of vertical-axis turbines is characterized by complex flow phenomena, including cyclic variations in the α, dynamic stall effects, and strong flow interference between the upwind and downwind passes of the blades. To address these challenges and to provide a computationally efficient predictive tool, Paraschivoiu [27] developed the Double-Multiple Stream Tube (DMST) theory—an extension of the classical momentum and blade element theories—specifically tailored for Darrieus-type vertical axis turbines.

The fundamental principle of the DMST model is based on dividing the turbine's swept area into several independent stream tubes, each representing a discrete section of the flow field. Within each stream tube, the conservation of momentum is applied separately to the upwind and downwind regions of the turbine, hence the term double stream tube. This dual treatment allows for distinct induced velocity distributions in both regions, reflecting the fact that the downstream flow has already been influenced by the energy extraction occurring in the upwind half.

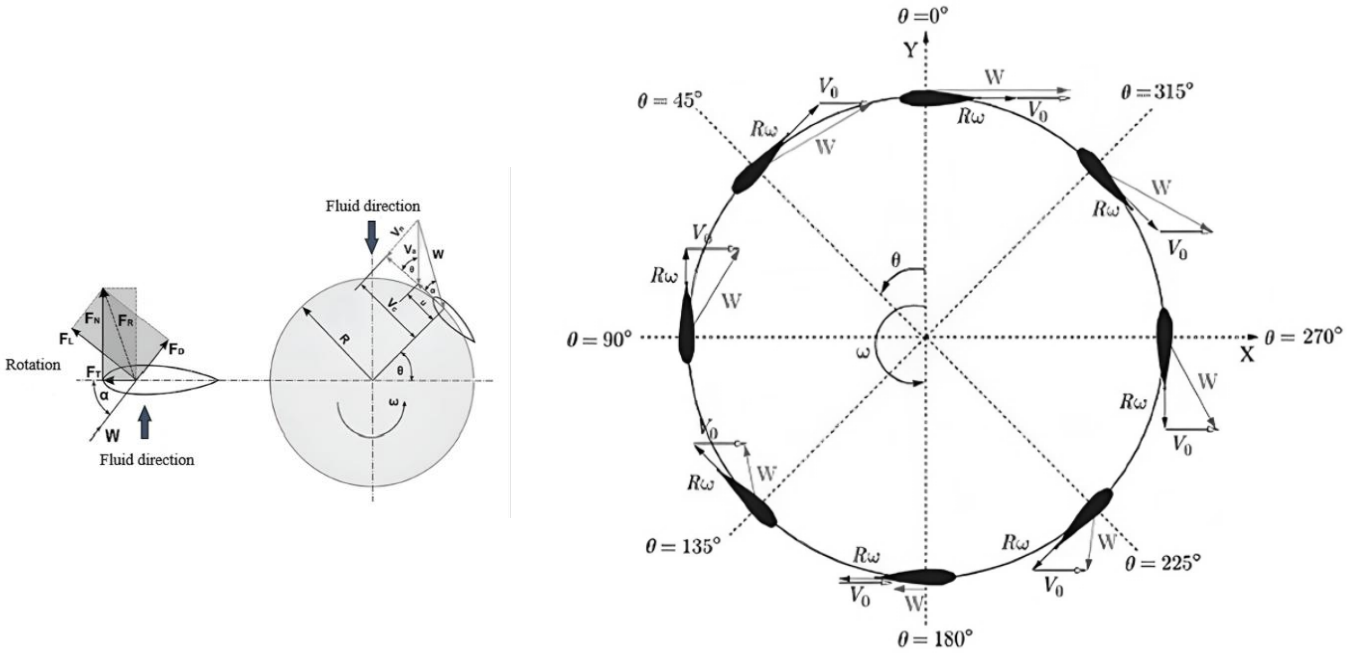

Fig. 15 Force and velocity vectors of a VAT [40] and Velocity vectors at different azimuth angles [41]

Each stream tube is analyzed independently, and the interaction between the aerodynamic forces generated by the blades and the local flow conditions is evaluated using a blade element approach. The local induced velocities are iteratively updated until the momentum balance between the air stream and the blade forces is satisfied. Through this iterative process, the model predicts the distribution of aerodynamic loads, torque, and power coefficients across the turbine's azimuthal positions.

This section investigates the impact of VG installation on the variation of energy extracted by the VACT, which is assumed to harness hydrokinetic energy from ocean currents. Figure 16 illustrates the preparation activities for the field trial of the BRIN vertical-axis ocean current turbine prototype conducted in 2014. In this study, the turbine prototype corresponds to the BRIN marine current turbine previously tested in the Madura Strait, Indonesia. The turbine, equipped with NACA 0021 blades, has a diameter (d) of 3.6 m, a span (s) of 2.18 m, and a chord length (c) of 0.18 m. During field testing, the turbine operated under ocean current velocities (v) ranging from 0.6 to 1.10 m/s, with a cut-in speed of 0.6 m/s and a total power coefficient of 37 %. Based on the field test conducted in the Madura Strait, Indonesia, the turbine generated 480 W of power at an ocean current velocity of 1.10 m/s [42].

Fig. 16 BRIN vertical-axis ocean current turbine prototype conducted in 2014 [43]

The 2014 field test of the marine current turbine was conducted using blades without VGs. In this study, it is demonstrated that integrating VGs with the turbine blades improves the flow characteristics around the

blades, thereby increasing lift and reducing drag. The enhancement of lift contributes to stall delay and an increase in turbine torque, which ultimately leads to an improvement in the power performance of the vertical-axis marine current turbine. Based on the predicted power enhancement, the addition of square-type VGs results in a 31.5 % increase in power output, yielding 631.2 W. Meanwhile, the installation of trapezoidal-type VGs provides a 29.5 % power increase, resulting in a power output of 621.6 W.

4. Conclusion

The placement of rectangular VGs at 10 %*c* proved to be the most effective in generating strong streamwise vortices, which delay flow separation, increase the C_L by up to 44.03 %, and reduce the C_D by up to 28.58 %. Meanwhile, trapezoidal VGs positioned at 15 %c also enhanced performance, increasing the C_L by 41.16 % and reducing the C_D by 25.44 %. However, the performance improvement with trapezoidal VGs was not as significant as that achieved with rectangular VGs. Although trapezoidal VGs also provide significant performance improvements, their effectiveness is slightly lower compared to rectangular VGs. This difference is likely due to variations in the vortex strength produced and their interaction with the airflow over the hydrofoil surface. These findings confirm that both the shape and placement of VGs play a critical role in flow control and in improving the hydrodynamic efficiency of the hydrofoil.

At low α = 0-10°, all configurations exhibit similar pressure distribution patterns. However, as the angle increases to moderate and high values (15-40°), notable differences emerge. The presence of VGs leads to increased pressure on the pressure side and decreased pressure on the suction side of the hydrofoil. This indicates that VGs effectively alter the flow by generating vortices that enhance energy within the boundary layer. These vortices help prevent or delay flow separation, a phenomenon typically responsible for the significant performance degradation of hydrofoils at high α (stall).

The analysis of flow separation behavior on the NACA 0021 hydrofoil demonstrates that the incorporation of VGs effectively delays stall and improves overall aerodynamic performance. At α, the clean hydrofoil exhibits extensive flow separation, leading to early stall. In contrast, the presence of VGs—particularly the square-type configuration placed at 10 % of the chord length—successfully maintains attached flow over a larger surface area by shifting the separation point further downstream. This delay in flow separation results in a higher C_L and reduced C_D, thereby enhancing the hydrodynamic efficiency of the turbine.

In the hydrofoil without VGs, the boundary layer lacks sufficient energy to remain attached to the surface as the α increases, leading to early separation and a sharp drop in lift, commonly referred to as stall. Conversely, hydrofoils equipped with VGs can control boundary layer behavior by generating streamwise vortices. These vortices energize the boundary layer, enabling it to better withstand adverse pressure gradients. As a result, the flow remains attached over a larger portion of the hydrofoil surface, delaying the onset of separation. This delay enhances hydrodynamic performance, particularly at moderate to high α, by maintaining lift and reducing performance losses associated with stall.

ACKNOWLEDGMENTS

The first author specifically expressed his deepest appreciation to the National Research and Innovation Agency of the Republic of Indonesia which funded this project through a scheme called The Education of Degree by Research Doctoral Program, based on the decree of the Deputy for Human Resources in Science and Technology (SDM IPTEK), No. 27/II/HK/2024. This article is one of the targets that must be achieved in implementing the Degree by Research Doctoral Program.

FUNDING

This research did not receive any external funding. Er. gratefully acknowledge the National Research and Innovation Agency of the Republic of Indonesia (BRIN) for supporting this research through the “Rumah Program” scheme of the Research Organization for Energy and Manufacture (OREM), Grant No. 56/III.3/HK/2003.

REFERENCES

[1] Kirke, B. K., Lazauskas, L., 2011. Limitations of fixed pitch Darrieus hydrokinetic turbines and the challenge of variable pitch. *Renewable Energy*, 36(3), 893-897. https://doi.org/10.1016/j.renene.2010.08.027

[2] Khan, M. J., Bhuyan, G., Iqbal, M. T., Quaicoe, J. E., 2009. Hydrokinetic energy conversion systems and assessment of horizontal and vertical axis turbines for river and tidal applications: A technology status review. *Applied Energy*, 86(10), 1823-1835. https://doi.org/10.1016/j.apenergy.2009.02.017

[3] Jirásek, A., 2005. Vortex-generator model and its application to flow control. *Journal of Aircraft*, 42(6), 1486-1491. https://doi.org/10.2514/1.12220

[4] Spalart, P. R., Shur, M. L., Strelets, M. K., Travin, A. K., 2015. Direct Simulation and RANS Modelling of a Vortex Generator Flow. *Flow, Turbulence and Combustion*, 95(2–3), 335-350. https://doi.org/10.1007/s10494-015-9610-8

[5] De Tavernier, D., Ferreira, C., Viré, A., LeBlanc, B., Bernardy, S., 2021. Controlling dynamic stall using vortex generators on a wind turbine airfoil. *Renewable Energy*, 172, 1194-1211. https://doi.org/10.1016/j.renene.2021.03.019

[6] Zhang, L., Li, X., Yang, K., Xue, D., 2016. Effects of vortex generators on aerodynamic performance of thick wind turbine airfoils. *Journal of Wind Engineering and Industrial Aerodynamics*, 156, 84-92. https://doi.org/10.1016/j.jweia.2016.07.013

[7] Utama, I. K. A. P., Satrio, D., Mukhtasor, M., Atlar, M., Shi, W., Hantoro, R., Thomas, G., 2020. Numerical simulation of foil with leading-edge tubercle for vertical-axis tidal-current turbine. *Journal of Mechanical Engineering and Sciences*, 14(3), 6982-6992. https://doi.org/10.15282/jmes.14.3.2020.02.0547

[8] Taylor, H. D., 1947. The elimination of diffuser separation by vortex generators. *Research department report no. r-4012-3, United Aircraft Corporation, East Hartford, Connecticut*, 103.

[9] Li, X. K., Kang, S. , Dai, L. P., Jiao, J. D., 2015. Effects on airfoil flow field by structure of vortex generators. *Kung Cheng Je Wu Li Hsueh Pao/Journal of Engineering Thermophysics*, 36(2), 326-329.

[10] Georgilidakis, S., 2022. NASA Puts New Twist on Vortex Generators? https://mentourpilot.com/nasa-puts-new-twist-on-vortex-generators/ (accessed 17th March 2026)

[11] Zhao, Z., Wang, D., Wang, T., Shen, W., Liu, H., Chen, M., 2022. A review: Approaches for aerodynamic performance improvement of lift-type vertical axis wind turbine. *Sustainable Energy Technologies and Assessments*, 49, 101789. https://doi.org/10.1016/j.seta.2021.101789

[12] Manolesos, M., Voutsinas, S. G., 2015. Experimental investigation of the flow past passive vortex generators on an airfoil experiencing three-dimensional separation. *Journal of Wind Engineering and Industrial Aerodynamics*, 142, 130-148. https://doi.org/10.1016/j.jweia.2015.03.020

[13] Zhao, Z., Zeng, G., Wang, T., Xu, B., Zheng, Y., 2016. Numerical research on effect of transition on aerodynamic performance of wind turbine blade with vortex generators. *Journal of Renewable and Sustainable Energy*, 8(6). https://doi.org/10.1063/1.4972888

[14] Rahuna, D., Erwandi, E., Satrio, D., Utama, I. K. A. P., 2024. Opportunities for Utilizing Vortex Generators on Vertical Axis Ocean Current Turbines: A Review. *The 4th Sustainability and Resilience of Coastal Management* (SRCM 2023), November 29, Surabaya, Indonesia, 89, 10003. https://doi.org/10.1051/bioconf/20248910003

[15] Galera, L., Martinez-Filgueira, P., Fernández-Gámiz, U., Zulueta, E., Lopez, J. M., Blanco, J. M., 2019. A triangular vortex generator modeling on a DU97-W-300 airfoil by a source term model. *Proceedings of the Institution of Mechanical Engineers, Part A: Journal of Power and Energy*, 233(5), 635-645. https://doi.org/10.1177/0957650919850449

[16] Müller-Vahl, H., Pechlivanoglou, G., Nayeri, C., Paschereit, C., 2012. Vortex Generators for Wind Turbine Blades: A Combined Wind Tunnel and Wind Turbine Parametric Study. *Proceedings of the ASME Turbo Expo*, June 11-15, Copenhagen, Denmark, 44724, 899-914. https://doi.org/10.1115/GT2012-69197

[17] Baldacchino, D., Ferreira, C., De Tavernier, D., W. Timmer, A., van Bussel, G. J. W., 2018. Experimental parameter study for passive vortex generators on a 30% thick airfoil: Experimental parametric vortex generator study. *Wind Energy*, 21(9), 745-765. https://doi.org/10.1002/we.2191

[18] Wang, H., Zhang, B., Qiu, Q., Xu, X., 2017. Flow control on the NREL S809 wind turbine airfoil using vortex generators. *Energy*, 118, 1210-1221. https://doi.org/10.1016/j.energy.2016.11.003

[19] Yan, Y., Avital, E., Williams, J., Cui, J., 2019. CFD analysis for the performance of micro-vortex generator on aerofoil and vertical axis turbine. *Journal of Renewable and Sustainable Energy*, 11(4). https://doi.org/10.1063/1.5110422

[20] Satrio, D., Erwandi, E., Rahuna, D., 2025. Investigation of enhanced peak lift performance and stall angle delay by attachment of Vortex Generators on blade surfaces of Vertical Axis Ocean Current Turbine. *Ocean Engineering*, 326, 120762. https://doi.org/10.1016/j.oceaneng.2025.120762

[21] Liang, L., Baoji, Z., Hao, Z., Hailin, T., Weijie, W., 2023. Hydrodynamic performance optimization of marine propellers based on fluid-structure coupling. *Brodogradnja*, 74(3), 145-164. https://doi.org/10.21278/brod74308

[22] Kale, F. M., Yilmaz, N., Sokmen, K. F., Shi, W, 2025. Experimental and numerical investigations of hydrodynamic performance for horizontal-axis hydrokinetic turbines. *Brodogradnja*, 76(3), 76308. https://doi.org/10.21278/brod76308

[23] Moon, H., Jeong, J., Park, S., Ha, K., Jeong, J. H., 2023. Numerical and experimental validation of vortex generator effect on power performance improvement in MW-class wind turbine blade. *Renewable Energy*, 212, 443-454. https://doi.org/10.1016/j.renene.2023.04.104

[24] Seifi Davari, H., Botez, R. M., Seify Davari, M., Chowdhury, H., Hosseinzadeh, H., 2024. Numerical and experimental investigation of Darrieus vertical axis wind turbines to enhance self-starting at low wind speeds. *Results in Engineering*, 24, 103240. https://doi.org/10.1016/j.rineng.2024.103240

[25] Troldborg, N., Zahle, F., Sørensen, N. N., 2015. Simulation of a MW rotor equipped with vortex generators using CFD and an actuator shape model. *53rd AIAA Aerospace Sciences Meeting*, January 5-9, Kissimmee, Florida, USA. https://doi.org/10.2514/6.2015-1035

[26] Rahuna, D., Erwandi, E., Kasharjanto, A., Suyanto, E. M., Mintarso, C. S. J., 2023. Experimental Study on Hydrodynamic Aspects of Turbine which Convert Hydrokinetic and Potential Coastal Wave Energy. *The 7th International Conference on Marine Technology* (SENTA 2022), October 20, Surabaya, Indonesia, 1166(1), 012021. https://doi.org/10.1088/1755-1315/1166/1/012021

[27] Paraschivoiu, I., 2002. Wind turbine design with emphasis on Darrieus concept. *Presses internationales Polytechnique*, Canada. https://doi.org/10.1515/9782553015946

[28] Della Posta, G., Martelli, E., Salvadore, F., Bernardini, M., 2024. High-fidelity simulations of microramp-controlled shock wave/boundary layer interaction. *Journal of Fluid Mechanics*, 998, A12. https://doi.org/10.1017/jfm.2024.742

[29] Schlichting , H., Gersten, K., 2016. Boundary-layer theory, 9th ed. *Springer*. https://doi.org/10.1007/978-3-662-52919-5

[30] Anderson, J., 2016. Fundamentals of aerodynamics (6th ed.), Columbus, OH: *McGraw-Hill Education*.

[31] Roache, P. J., 1994. Perspective : A Method for Uniform Reporting of Grid Refinement Studies. *Journal of Fluids Engineering-ASME*, 116(3), 405-413. https://doi.org/10.1115/1.2910291

[32] Holst, D., Church, B., Wegner, F., Pechlivanoglou, G., Nayeri, C. N., Paschereit, C. O., 2019. Experimental Analysis of a NACA 0021 Airfoil under Dynamic Angle of Attack Variation and Low Reynolds Numbers. *Journal of Engineering for Gas Turbines and Power*, 141(3), 031020. https://doi.org/10.1115/1.4041146

[33] Holst, D., Church, B., Pechlivanoglou, G., Tüzüner, E., Saverin, J., Nayeri, C.N., Paschereit, C.O., 2019. Experimental analysis of a NACA 0021 airfoil section through 180-deg angle of attack at low Reynolds numbers for use in wind turbine analysis. *Journal of Engineering for Gas Turbines and Power*, 141(4), 041012. https://doi.org/10.1115/1.4041651

[34] Sheldahl, R. E., Klimas, P. C., 1981. Aerodynamic characteristics of seven symmetrical airfoil sections through 180-degree angle of attack for use in aerodynamic analysis of vertical axis wind turbines. *Energy Report*, Sandia National Laboratories. https://doi.org/10.2172/6548367

[35] Roache, P. J., 1998. Fundamentals of Verification and Validation, 2009th ed. *hermosa*, Socorro, New Mexico 87801.

[36] ITTC, 1999. CFD Verification, *ITTC – Recommended Procedures and GuidelinesProcedures and Guidelines*, 485-487.

[37] Celik, I. B., Ghia, U., Roache, P. J., Freitas, C. J., 2008. Procedure for Estimation and Reporting of Uncertainty Due to Discretization in CFD Applications, *Journal of Fluids Engineering, Transactions of the ASME*, 130(7), 078001. https://doi.org/10.1115/1.2960953

[38] Zhu, C., Chen, J., Qiu, Y., Wang, T., 2021. Numerical investigation into rotational augmentation with passive vortex generators on the NREL Phase VI blade. *Energy*, 223, 120089. https://doi.org/10.1016/j.energy.2021.120089

[39] Wei, Y., Zhang, J., Liu, K., Pan, J., Zhang, L., Chen, W., Zhang, Q., 2025. Numerical study of the influence of hydrofoil hydrodynamic performance considering near-free surface, *Brodogradnja*, 76(1), 76108. https://doi.org/10.21278/brod76108

[40] Mohamed, M. H., 2012. Performance investigation of H-rotor Darrieus turbine with new airfoil shapes, *Energy*, 47(1), 522-530. https://doi.org/10.1016/j.energy.2012.08.044

[41] Ghasemian, M., Ashrafi, Z. N., Sedaghat, A., 2017. A review on computational fluid dynamic simulation techniques for Darrieus vertical axis wind turbines. *Energy Conversion and Management*, 149, 87-100. https://doi.org/10.1016/j.enconman.2017.07.016

[42] Kasharjanto, A., Rahuna, D., Rina, D., 2017. Study on the Implementation Of Marine Current Energy In Indonesia. *Jurnal Ilmiah Teknologi Maritim*, 11(2), 75-84. https://doi.org/10.29122/jurnalwave.v11i2.3070

[43] Badan Riset dan Inovasi Nasional (BRIN), 2014. Field testing of a 10kW ocean current power plant under the Suramadu Bridge, Madura Strait, *Internal Report - BPPT Research DIPA - 2014*.